Research Square

Preprints are preliminary reports that have not undergone peer review.
They should not be considered conclusive, used to inform clinical practice,
or referenced by the media as validated information.

Sedimentary evidence of limnic eruptions in Lake Monoun, West Cameroon

Amin Mouhamed

aminnsang7@gmail.com

University of Liege

Article

Keywords: Lake Nyos-type, lacustrine sediment, paleolimnology, natural hazards, degassing

Posted Date: May 13th, 2026

DOI: https://doi.org/10.21203/rs.3.rs-9481796/v1

License: This work is licensed under a Creative Commons Attribution 4.0 International License.
Read Full License

Additional Declarations: There is **NO** Competing Interest.

Abstract

Limnic eruptions, involving the sudden release of carbon dioxide (CO_2) clouds from lakes, caused catastrophic disasters at Lakes Monoun and Nyos in the mid-1980s, killing nearly 2,000 people. Yet direct evidence of the conditions preceding, accompanying, and following such events has remained lacking. Here we present the first reconstruction of a limnic eruption from a multiproxy analysis of a sediment core from Lake Monoun. We show that an increase in siderite abundance in the sediments, linked to the rising dissolved CO_2 concentration in the lake, preceded the eruption. By the mid-1960s, CO_2 accumulation had displaced the chemocline to shallower than 25 m depth. Furthermore, a pure siderite layer associated with the 1984 event records maximum gas saturation, and the event was followed by a decline in CO_2-related geochemical signals. We also identified eight other likely degassing episodes over the past ~ 500 years.

Introduction

First recognized in the mid-1980s, limnic eruptions are a rare geological hazard with potentially catastrophic consequences. They occur when dissolved carbon dioxide (CO_2) is abruptly released from volcanic lakes as a cloud denser than the ambient air, posing a severe threat to surrounding populations[1]. In August 1984, such an event in Lake Monoun (Cameroon) killed 37 people by asphyxiation. Two years later, a similar but more intense disaster at Lake Nyos claimed more than 1,800 lives. The scale, suddenness, and severity of these tragedies drew global attention to the geochemical and limnological conditions that govern gas accumulation and abrupt degassing in volcanic lakes. Sigurdsson et al.[1] first described the eruptive mechanism at Lake Monoun and subsequently extended it to Lake Nyos. Continued monitoring after these disasters revealed persistent CO_2 recharge into both lakes[2–4], supporting spontaneous degassing as the most plausible eruption mechanism, thus requiring neither external (earthquakes, landslides, wind forcing) nor internal triggers (subaqueous mass movements, internal waves). These findings also highlighted the likelihood of future recurrences[5, 6].

Risk assessment has relied largely on dissolved gas chemistry in the water column, whereas mitigation has been achieved through continuous artificial degassing[7]. In parallel, large-scale diagnostic surveys based on repeated measurements of dissolved CO_2 in volcanic lakes, particularly stratified maar lakes, have been conducted worldwide, notably at Lakes Albano[8–10], Monticchio[11,12], and Averno[12,13] (Italy), Pavin (France)[14,15], Laacher See (Germany)[16,17], Lake Kivu (Democratic Republic of the Congo)[13,18], and Río Cuarto and Laguna Hule (Costa Rica)[19]. All investigated lakes have CO_2-rich deep waters, but the potential for limnic eruptions in these systems remains debated, largely because most are located in temperate regions where recurrent water-column overturn limits long-term gas accumulation at depth[10,20]. Nonetheless, modern monitoring alone is insufficient to assess the long-term behavior, recurrence, and sedimentary expression of conditions associated with limnic eruptions. Sedimentary archives therefore offer a critical complementary approach for identifying past degassing events and reconstructing the processes that preceded them.

More than 40 years after the limnic eruptions at Lakes Nyos and Monoun, the sedimentary records of these two maar lakes in the Cameroon Volcanic Line (Fig. 1a)[21,22] have yet to be examined for evidence of past limnic eruptions.

Here, we examine the sedimentary archive of Lake Monoun (1080 m a.s.l. in the western Noun Plain)[6]. The lake comprises three crater sub-basins, including the larger and deeper eastern basin (~ 100 m deep) where active degassing presently occurs[23–25]. Focusing on this basin, we aim to identify sedimentological, mineralogical, and geochemical proxies of the 1984 limnic eruption, refine the limnic eruption mechanism based on sedimentary evidence, and assess the occurrence of past limnic eruptions. More broadly, this study highlights the potential of sedimentary archives to extend hazard assessments beyond contemporary monitoring and provide a longer-term framework for understanding limnic eruption dynamics in volcanic lakes worldwide.

Results

Sedimentology

Core LMo23-2 was retrieved from the eastern basin in 2023 at a water depth of 25 m, above the 2015 chemocline (C2, Fig. 1c) and near the depth of the 2003 chemocline (C1, Fig. 1c)[24,26]. The core was subdivided into four units on the basis of sedimentological features (Fig. 1d) observed in the split-core surface and X-ray computed tomography (CT) imagery, together with organic-matter content (OM; 7–37%) and magnetic susceptibility (MS; 10–1000 × 10^{-5} SI).

Unit 1 (110–79 cm depth in core) consists of reddish to yellowish sediments intercalated with dark greenish to blackish deposits and is characterized by strongly fluctuating MS and OM values. Between 107 and 94 cm, the laminated sediments are disturbed and are interpreted as a mass-transport deposit (e.g., Schnellmann et al.[27]). At 89–88 cm, a coarse white layer with sharp boundaries and high MS may represent a tephra layer, although this remains to be confirmed. Between 85 and 81 cm, a sand-filled fault fracture, probably induced during coring, is clearly visible in the CT imagery due to its high radiodensity; it appears to originate from a sand bed forming the base of a turbidite between 81 and 79 cm depth (Fig. 1e). This gray-green turbidite displays normal grading, with sand grains concentrated at its base, consistent with the observed decrease in radiodensity and increase in MS. The high MS and low OM values of this unit indicate its dominantly clastic composition.

Unit 2 (79–52 cm) is characterized by yellowish to reddish laminated sediments that become darker and more greenish upwards. Above 75 cm, this color change is accompanied by decreasing radiodensity, declining MS values (250–15 × 10^{-5} SI) and increasing OM content (18–25%).

Unit 3 (52–27 cm) is composed of brown-red sediments that become lighter upwards. Lamination is moderately developed towards the top, although it is visible throughout the unit in the CT data. Unit 3 is characterized by relatively stable MS values (20–45 × 10^{-5} SI) and OM content (~ 20%).

Unit 4 (27–0 cm) is faintly laminated and consists of dark sediments interrupted by yellowish and reddish layers at 9–6 cm and 4–3 cm. It is characterized by fluctuating MS values (10–200 × 10^{-5} SI) and an overall increase in OM content (20–40%), reaching the highest values in the record. Peaks in OM content, together with troughs in MS, are associated with dark deposits, whereas the decreased OM content between 14.5 and 6.5 cm coincides with a gradual increase in MS, culminating in the reddish layer between 9.5 and 6.5 cm.

Age model

In core LMo23-2, the excess ^{210}Pb ($^{210}Pb_{xs}$) activity ranges from 2 to 210 mBq g^{-1} and decreases downcore (Fig. 2a), reaching negligible levels at 49.5 cm depth in core. Anomalously high values in the intervals 15.5–13.5 cm (377–577 mBq g) and 5–4.5 cm (118 mBq g^{-1}) disrupt the expected exponential $^{210}Pb_{xs}$ decay profile (Fig. 2a) and coincide with depths marked by high OM content (> 20%) and mineralogical changes described in the **Bulk mineralogy** subsection. These intervals were excluded from the sediment accumulation rate (SAR) calculation.

^{232}Th activity ranges from 2 to 49 mBq g^{-1} and increases downwards (Fig. 2a), consistent with the sedimentary changes described above. Accordingly, the $^{210}Pb_{xs}$ profile was normalized against ^{232}Th to account for these changes.

The ^{232}Th-normalized $^{210}Pb_{xs}$ profile yields an average SAR of ~ 2.45 mm yr^{-1} for the upper 50 cm of the core. The ^{137}Cs activity peak, corresponding to maximum nuclear fallout in 1963, occurs at a depth of 15 cm (Fig. 2a) and is consistent with this age model.

The Bayesian age model for core LMo23-2, which is constrained by the year of core recovery (2023), ^{210}Pb and two ^{14}C ages (Table 1), indicates that the sequence spans the last ~ 500 years (Fig. 2b). The lower ^{14}C sample was obtained from the mass-transport deposit (MTD) and only provides a maximum age. Nevertheless, we include it because it is consistent with the sedimentation rates inferred from the upper half of the core.

Table 1
Radiocarbon ages and calibrated age ranges (95.4% probability).

Lab code	Core	Depth (cm)	^{14}C age (yr BP)	Cal age (CE)	Midpoint cal (CE)
GdA-7877.1.1	LMo23-2	50–51	231 ± 20	1640–1673.34 (51.5%) 1743.1–1750.32 (1.4%) 1765.8–1773.9 (2.2%) 1777.98–1798.9 (35.4%)	1656.5 ± 33
GdA-7879.1.1	LMo23-2	93.5–94.5	478 ± 43	1326–1350 (2.8%) 1394–1487 (92.6%)	1440.5 ± 94
GdA-7878.1.1	LMo23-1	71–72	1.3499 ± 0.003	1962.62–1962.78 (3.9%) 1975.94–1977.06 (83.8%) 1977.38–1977.68 (7.8%)	1969.5 ± 15
GdA-7880.1.1	LMo23-1	101–102	191 ± 20	1660.1–1686.82 (20.8%) 1730.98–1807.26 (56.8%) 1926.1 (17.8%)	1795 ± 250

Bulk mineralogy

Mineralogies derived by X-ray diffraction reveal the presence of carbonates (siderite), clay minerals (kaolinite/dickite), silicates (quartz, orthoclase, anorthite), and oxides/hydroxides (hematite, gibbsite, anatase). Principal component analysis (PCA) shows an inverse relationship between siderite and all other minerals (Supplementary Fig. 1a), suggesting that variations in siderite content largely control the relative abundance of the other mineral phases. Moreover, siderite abundance varies strongly throughout the core (Fig. 3), a pattern that is particularly well captured by the siderite/kaolinite ratio (Supplementary Fig. 2). Nine intervals in core LMo23-2 are characterized by siderite contents exceeding an arbitrary threshold of 35% and are commonly followed by an abrupt decline; these are hereafter referred to as siderite episodes SE1 to SE9 (Fig. 3).

Units 1 and 2 together (1500–1769 CE-) contain SE1–SE6, with maximum siderite abundances of 40–60%. Hematite is preferentially observed during SE1 to SE4, although only in minor amounts. Notably,

SE2 and SE3 occur immediately above the MTD and the turbidite, respectively. In Unit 3 (1769–1910 CE), no siderite episodes are observed, and siderite abundances remain relatively low and stable, increasing gradually from 2% at 52 cm depth in core to 20% at 40 cm, then declining progressively to 10% at the top of the unit. Unit 4 (1910–2023 CE) is marked by three siderite-rich intervals at 27–17 cm (SE7), 15–6 cm (SE8), and 5–3 cm (SE9). During SE7 (1910–1945 CE), siderite abundances increase progressively from 10% to 35% between 27 and 20 cm, then decrease back to 10% at 17 cm. SE8 (1965–1990 CE) is characterized by the highest siderite abundances in the core, ranging from 70% to 100% at 9 cm (~ 1984 CE), before dropping to 40% at 6 cm. SE9 (2001–2009 CE) shows an increase in siderite from 45% to 80% at 4 cm, followed by an upwards decrease to 30%.

Elemental geochemistry

X-ray fluorescence core-scanning data reveal marked geochemical variability, notably in the relative abundances of Fe, S, Ca, and Ti (Fig. 4). Principal component analysis (PCA) identified two dominant components that together account for 81.5% of the total variance. Element loadings define two main groups: Al, Ti, Zr, and Rb in the first, Fe, Br, S, Cl, and Ca in the second (Supplementary Fig. 1b).

Across SE1 to SE6 (Units 1 and 2), higher Fe abundances are associated with lower S and Ti abundances and Ca/Fe ratios. Fe abundances remain relatively stable during the two oldest episodes (SE1 and SE2) but increase progressively from SE3 to SE6. In Unit 4, the center of Fe-rich interval SE8 (~ 9.5 cm; ~1984 CE) coincides with a sharp decline in S abundance (purple band, Fig. 4).

Discussion

The significance of siderite

Siderite, an iron carbonate ($FeCO_3$), occurs in both marine and lacustrine environments and has previously been used as a paleoenvironmental proxy because its formation depends on specific environmental conditions[28–30]. Authigenic siderite precipitation occurs when reduced iron (Fe^{2+}) reacts with dissolved inorganic carbon, mainly in the form of carbonate (CO_3^{2-}) or bicarbonate (HCO_3^-), within an anoxic ferruginous redox window. This process is favored under neutral to slightly alkaline conditions, low sulfur availability (which limits the preferential formation of iron sulfides), and low Ca/Fe ratios (which reduce competition with calcium carbonates)[30–32]. In CO_2-rich systems, the dissolution of CO_2 increases bicarbonate availability and can enhance alkalinity once acidity is buffered by processes such as silicate weathering, microbial activity, or mixing with alkaline lake waters[33]. The reduced iron involved in siderite formation may derive from microbial Fe(III) reduction during early diagenesis, as well as from deep fluid inputs in volcanic lake settings[16,30,31].

Lake Monoun provides favorable conditions for authigenic siderite formation. The maar lake is characterized by deep CO_2 degassing, reflecting magmatic gas recharge, as indicated by the ^{13}C isotopic

composition of bicarbonate and CO_2 measured in the deep water column[1,31,34]. Mineralogical and geochemical data further suggest that siderite is not controlled by the same processes as the detrital sediment fraction. Principal component analysis of both mineralogical (Supplementary Fig. 1a) and geochemical data (Supplementary Fig. 1b) indicates that siderite, interpreted here as an authigenic phase, is decoupled from the processes controlling the other minerals.

The association of Fe with elements commonly linked to organic matter, such as Br, Cl, and S[35], points to a connection with water-column productivity and internal lake processes (Supplementary Fig. 1b). By contrast, Al, Ti, Zr, and Rb define a detrital fraction dominated by silicates and oxides (identified by XRD) and delivered to the lake from the watershed through surface runoff. Among the silicates, the dominance of kaolinite is consistent with the tropical setting of the watershed, where it forms under moderate hydrolysis in warm and humid conditions[36]. In addition to this detrital kaolinite supply, Rietveld refinement suggests a minor contribution from dickite, a high-temperature kaolinite polytype[37]. The presence of this distinctive clay phase is consistent with the volcanic setting and the circulation of hot fluids.

These observations support an authigenic origin of siderite in Lake Monoun sediments and suggest that its abundance records internal geochemical changes in the lake, potentially linked to variations of CO_2 input.

Sedimentary evidence of the 1984 limnic eruption

Distinct mineralogical and geochemical changes are observed between 15 and 6 cm depth in core (1965–1990 CE) in Lake Monoun sediments (Fig. 5), an interval encompassing the 1984 limnic eruption. According to the age model (Fig. 2), the layer between 9.5 and 10.5 cm is dated to 1983 ± 5 years. The highest siderite abundance (100%; SE8) occurs between 10 and 9 cm, consistent with the age of the 1984 limnic event. This abrupt shift in mineral assemblage coincides with increased Fe and decreased OM contents, suggesting that, at least in the siderite-rich layers, iron was not solely associated with organic matter but may also have been supplied by ascending volcanic fluids[16]. In addition, the low Ca/Fe ratio (Fig. 5) would have favored siderite precipitation over calcite[31].

Prior to the 1984 limnic eruption, siderite, Fe, S, and Ca abundances increased and remained elevated since 1965 (15–9.5 cm) (Fig. 5). We interpret this interval as a precursor phase to the limnic eruption. At the coring depth, the mineralogical and geochemical data indicate reducing conditions and high dissolved CO_2 contents consistent with strong water-column stratification and a chemocline positioned shallower than 25 m, that is, above the core site.

The maximum siderite abundance (100%) indicates a period during which the system reached saturation with respect to Fe^{2+} and dissolved inorganic carbon. The abrupt decrease in S abundance at 9 cm depth suggests rapid reorganization of the water column accompanied by oxygenation, and thus a disruption of stratification, which we interpret as the sedimentary imprint of the limnic eruption. Residual CO_2 would

then have been released to the atmosphere during collapse of the chemocline, triggering abrupt water-column mixing. The concomitant decreases in siderite, Fe, and Ca abundances, alongside increases in S and OM abundances between 9 and 6 cm, indicates a gradual return to pre-1965 conditions and thus the re-establishment of the chemocline > 25 m depth.

Updated model for limnic eruptions

Following the 1984 limnic eruption at Lake Monoun, Sigurdsson et al.[1] proposed a limnic eruption mechanism that was later extended to Lake Nyos. More recently, Ohba et al.[24] proposed a model integrating bathymetric data[23] with water chemistry changes from the day after the eruption to 2015[26]. This model highlights two large depressions at the lake bottom (D1 and D2, with D1 being more active; Fig. 1b), interpreted as discharge points for ascending warm (24°C), acidic (pH 5.67), CO_2-rich fluids. CO_2-rich water, emitted mainly through D1, is then redistributed horizontally within the hypolimnion, contributing to gradual gas accumulation or recharge below the chemocline, estimated at ~ 50 m depth. According to this model, gas bubbles themselves may contribute to destabilizing the system and promoting rapid CO_2 releases.

Here, we propose an updated conceptual model for limnic eruptions based on mineralogical and geochemical data from core LMo23-2, retrieved at 25 m water depth in Lake Monoun. The occurrence of several siderite-rich episodes suggests repeated periods of CO_2 build-up in the lake, possibly punctuated by episodes of degassing. The model comprises four stages, as illustrated in Fig. 6.

- Stage 1 (Fig. 6a) corresponds to ca. 1952–1961. Magmatic CO_2-rich fluids ascend along the annular fault of the diatreme and enter the lake bottom through depression D1. At this stage, the chemocline was likely deeper than 25 m, consistent with the model of Ohba et al.[24]. As gas accumulated in the hypolimnion and approached saturation, gas bubbles may have remained longer in the water column.
- Stage 2 (Fig. 6b) corresponds to the period around 1965, when continued CO_2 influx may have displaced the chemocline to shallower than 25 m depth. At the coring site, this transition is associated with enhanced siderite deposition, consistent with increased dissolved CO_2 content.
- Stage 3 (Fig. 6c) spans the interval between 1965 and 1984. Continued CO_2 influx likely led to progressive saturation of the system and increasingly reducing conditions in the water column, favoring increased siderite precipitation in the sediment. We infer that the chemocline rose further towards the surface, possibly reaching ~ 15 m depth shortly before the limnic eruption. This position is consistent with the chemocline inferred by Sigurdsson et al.[1] from oxygen isotopes and is shallower than that proposed in the previous model of Ohba et al.[24]. At this stage, siderite reached its maximum abundance, recording peak CO_2 sequestration in the sediment.
- Stage 4 (Fig. 6d) corresponds to the limnic eruption itself. Gas pressure likely destabilized the chemocline and the water-column stratification, leading to rapid mixing of the water layers and the

release of CO_2 towards the atmosphere. This sudden release may have generated surface waves and laterally dispersed CO_2-rich clouds over the surrounding land. After the eruption, the lake returned to a more stable state, with the re-establishment of the chemocline at greater depth (~ 60 m according to Ohba et al.[24]).

Potential recurrence of limnic eruptions

After identifying the sedimentary signatures of the 1984 limnic eruption, we use them here as a reference framework to interpret potential past degassing episodes in Lake Monoun. The observation of a chemocline at around 25 m depth in 2003[24], corresponding to SE9 in our sediment core, further supports this approach. The identified intervals show a geochemical evolution broadly similar to that observed before and after the 1984 event, although with variable intensities. Taken together, these observations suggest repeated episodes of strong stratification and displacement of the chemocline toward shallower depths due to CO_2 recharge, followed by system destabilization, CO_2 release, and mixing of the water masses. Six episodes (SE1–SE6) occurred between ~ 1500 and ~ 1750 CE (Units 1 and 2), whereas three others (SE7–SE9) occurred in the last century, between ~ 1900 and 2010 CE (Unit 4) (Figs. 3, 4).

The intensity of CO_2 accumulation below the chemocline when shallower than 25 m appears to vary among these SEs. This interpretation is consistent with the hypothesis of Sigurdsson et al.[1] that, if CO_2 accumulation is gradual, each additional input should increase siderite supersaturation. When accumulation reaches a high level, siderite records enhanced CO_2 sequestration prior to system destabilization and gas release. The abrupt decreases in siderite abundance observed at the ends of the episodes may therefore mark the onset of degassing. SE8, which corresponds to the 1984 event, represents the most extreme expression of this dynamic, characterized by a sediment wholly composed of siderite. The other SEs, whose peaks do not reach 100%, suggest intermediate levels of CO_2 accumulation. For example, SE9 shows siderite and Fe peaks consistent with a period of accumulation followed by a degassing episode. The relatively limited width of this episode suggests weaker or shorter-lived accumulation than during more strongly expressed episodes. This interpretation is consistent with the position of the chemocline at ~ 25 m depth in 2003[24]. Such limited accumulation may explain the non-catastrophic nature of this degassing event. By contrast, broader peaks may reflect longer accumulation episodes.

However, several processes may have prevented the sustained accumulation of gas in the water column, in relation to both stratification stability and the intensity of CO_2 recharge, thereby preventing the system from reaching maximum siderite saturation. One possibility is insufficiently stable stratification, as suggested by the coexistence of reduced and oxidized Fe-bearing phases[38], particularly during SE1–SE4. Other mechanisms of episodic destabilization may also be considered, including volcanic eruptions (Fig. 1e), the ejection of tephra containing siderite-rich sediments[34], and sedimentary disturbances such as the MTD and turbidite, respectively associated SE2 and SE3. Overall, these results suggest that Lake

Monoun has experienced recurrent episodes of CO_2 recharge, shallowing of the chemocline, and water-column destabilization over the past centuries. However, only the 1984 event clearly records the highest saturation level, which is consistent with a major limnic eruption. The sedimentary archive thus highlights both the variable intensity of these episodes and the value of sediments for reconstructing the history of past degassing. Whether climate change may have favored the exceptional accumulation recorded in 1984 by strengthening lake stratification remains an open question.

Conclusions

More than 40 years after the recognition of limnic eruptions, direct geological evidence capturing the conditions before, during, and after these disasters has remained lacking. Here, the sedimentary record of a short core (LMo23-2), retrieved at shallow depth (25 m) in Lake Monoun, provides a strong basis for refining the existing limnic eruption model. The main conclusions of this study are as follows.

- The presence of siderite and progressive increases in its abundance record reducing bottom-water conditions and high dissolved CO_2 contents, which were supplied by ascending magmatic fluids.
- The ^{210}Pb age model indicates that a pure siderite layer was deposited just prior to the 1984 limnic eruption, providing the first sedimentary record of such an event.
- The sedimentary archive of Lake Monoun reveals several siderite-rich layers, indicating recurrent degassing episodes over the past 500 years. These episodes vary in expression, reflecting variable degassing conditions linked to the gradual accumulation of dissolved CO_2 and the position of the chemocline. The 1984 event stands out as unprecedented over the past 500 years, during which only smaller episodes of gas buildup and release are inferred.
- The occurrence of an event after the 1984 limnic eruption (SE9, around 2003) shows that significant gas inputs may still occur in the lake. Although artificial degassing is currently employed to remove CO_2 from the lake, another limnic eruption remains possible if the CO_2 influx exceeds the removal capacity of the pumping system. Continuous monitoring of gas levels and lake dynamics is therefore essential to reducing future risks.
- More broadly, these results provide a reference framework for future research and monitoring of Nyos-type lakes worldwide. They also highlight the need to integrate climate-change dynamics into hazard assessment.

Materials and methods

Sediment coring and non-destructive analyses

In March 2023, two sediment cores were recovered from the main eastern basin of Lake Monoun (Fig. 1b) using a Uwitec® coring system equipped with a 90 mm diameter tube. Core LMo23-1 (120 cm long) was retrieved at a water depth of 45 m, whereas core LMo23-2 (110 cm long) was collected at 25 m water depth on a plateau. Both cores were scanned by X-ray CT at Ghent University Hospital (Siemens

SOMATOM Definition Flash, Siemens AG), with a spatial resolution of ~ 0.2 mm in the *x-y* plane and 0.3 mm in the *z* direction. Visualization and analysis were performed using VGStudio 3.2 and ImageJ, respectively.

The cores were then split lengthwise using a GEOTEK® core cutter, imaged by line scanning, and logged at 2 mm intervals for MS using a Bartington MS2E point sensor mounted on a GEOTEK® Multi-Sensor Core Logger at Ghent University (Ghent, Belgium).

Relative elemental geochemical variations were measured using a Scopix X-ray imaging system (58 kV, 10 mA) and an Avaatech X-ray fluorescence core scanner equipped with an Fe-Mo tube at the PACS platform of the EPOC laboratory, University of Bordeaux (Bordeaux, France). Measurements were performed on half-core sections at 10, 30, and 50 kV with exposure times of 15, 20, and 25 s, respectively.

Destructive analyses

Loss-on-ignition and bulk mineralogical analyses were performed on core LMo23-2. Subsamples of 1 cm^3 were collected at 1 cm intervals and oven-dried overnight at 105°C to determine water content and dry bulk density. Organic matter content was estimated by combustion at 550°C for 4 h, followed by estimation of inorganic carbonate content by heating at 950°C for 2 h[39].

Bulk mineralogy was determined by X-ray diffraction at an average sample spacing of 1 cm. Samples were ground using an agate mortar and pestle, sieved through a 150 µm mesh, and prepared following the back-loading method[40]. Unoriented powders were scanned over 2–70° 2θ with a step size of 0.009° 2θ and a counting time of 0.5 s per step using a Bruker® D8 Advance Eco diffractometer (Cu Kα radiation, λ = 1.5418 Å, 40 kV, 25 mA) coupled to a LynxEye Xe detector. Mineral phases were identified using Bruker® EVA software, and their relative abundances were estimated by Rietveld refinement using Bruker® TOPAS software.

Sediment dating

The activities of ^{210}Pb, ^{226}Ra, ^{232}Th, and ^{137}Cs were determined in the upper 50 cm of cores LMo23-1 and LMo23-2 by direct gamma spectrometry on ~ 2 g of dry sediment. Measurements were performed using a low-background, high-efficiency well-type gamma detector at the EPOC laboratory. Excess ^{210}Pb (^{210}Pb□□) activity was calculated by subtracting ^{226}Ra activity from total ^{210}Pb activity. Because excess both ^{210}Pb□□ and ^{226}Ra were observed in some layers, ^{210}Pb□□ was normalized to ^{232}Th to obtain $^{210}Pb_{xs}$ activities only influenced by decay/time and not changes in sediment composition. Also, because there are changes in sediment, the layers with high values are not taken into account in the calculation. The normalized values (^{210}Pb□□–^{232}Th) were used to calculate SAR using the constant flux/constant sedimentation model. SAR was then used to calculated ages. ^{137}Cs was used to check the validity of the ^{210}Pb-dervied age model.

To determine the ages of deeper sediments, four leaf fragments were sampled at 50–51 cm and 93.5–94.5 cm depth in LMo23-2 and at 71–72 cm and 101–102 cm in LMo23-1 (Table 1) for radiocarbon (^{14}C) analysis by accelerator mass spectrometry. Analyses were performed at the GADAM Centre, Silesian University of Technology (Gliwice, Poland). The ^{14}C ages were calibrated using the IntCal20 calibration curve for the Northern Hemisphere[41]. The ^{210}Pb and ^{14}C ages from LMo23-2 were then integrated into a Bayesian age-depth model using the Bacon 2.5.3 package[42] in R[43]. Two layers, at 82–79 cm and 102–93 cm, were identified as mass deposits and excluded from the age-depth model.

Declarations

Data availability

The data supporting the findings of this study are available within the paper and its Supplementary Information. Source data are available from the corresponding author upon reasonable request.

Acknowledgements

We thank the Lake Monoun degassing project team for their support during the coring campaigns, in particular Dr. Mouncherou Oumar Farouk, project coordinator, and Dr. Wilson Fantong, head of the scientific committee. We also thank Dr. Akono, Mr. Ngono, and the Lake Monoun fishermen for their assistance in the field. We are grateful to the staff of the EPOC laboratory at the University of Bordeaux, France, for discussions on geochemical interpretation. We particularly thank Léo Chassiot for his careful reading of the manuscript and valuable suggestions. Thanks to Dr. Soualiou Njimbouobouo and Gouban Hamadjida for helpful discussions during the preparation of the manuscript and figures.

Author contributions

A.N.M., D.R., and N.F. conceived the study. A.N.M. wrote the first draft of the manuscript and carried out the analyses. S.S carried out ^{210}Pb chronology. A.N.M. and M.V.D. carried out CT scanning and magnetic susceptibility measurements. A.N.M., R.S., and M.R. performed the Bayesian age-depth modelling and statistical analyses. All authors contributed to the interpretation of the results and to the writing and revision of the manuscript.

Competing interests

The authors declare no competing interests.

References

1. Sigurdsson H, Devine JD, Tchoua FM, Presser TS, Pringle MKW, Evans WC (1987) Origin of the lethal gas burst from Lake Monoun. J Volcanol Geotherm Res 31:1–16

2. Kusakabe M, Ohsumi T, Aramaki S (1989) Chemical and isotopic evidence from three Cameroonian crater lakes. J Volcanol Geotherm Res 39:167–185
3. Kusakabe M, Tanyileke G, McCord SA, Schladow SG (2000) Recent pH and CO_2 profiles at Lakes Nyos and Monoun. J Volcanol Geotherm Res 97:241–260
4. Evans WC, Kling GW, Tuttle ML, Tanyileke G, White LD (1993) Gas buildup in Lake Nyos: the recharge process and its consequences. Appl Geochem 8:207–221
5. Kusakabe M (2015) Evolution of CO_2 content in Lakes Nyos and Monoun. In: Rouwet D, Christenson BW, Tassi F, Vandemeulebrouck J (eds) Volcanic Lakes. Springer
6. Kusakabe M (2017) Lakes Nyos and Monoun gas disasters. Geochem Monogr Ser 1:1–50
7. Halbwachs M, Sabroux JC, Kayser G (2020) Final step of the 32-year Lake Nyos degassing adventure. J Afr Earth Sci 167:103575
8. Carapezza ML, Lelli M, Tarchini L (2008) Geochemistry of the Albano and Nemi crater lakes in the volcanic district of Alban Hills (Rome, Italy). J Volcanol Geotherm Res 178:297–304
9. Chiodini G, Tassi F, Caliro S, Chiarabba C, Vaselli O, Rouwet D (2012) Time-dependent CO_2 variations in Lake Albano associated with seismic activity. Bull Volcanol 74:861–871
10. Rouwet D, Chiodini G, Ciuccarelli C, Comastri A, Costa A (2019) Lago Albano, the anti-Nyos-type lake. J Afr Earth Sci 150:425–440
11. Caracausi A, Nicolosi M, Nuccio PM, Favara R, Paternoster M, Rosciglione A (2013) Geochemical insight into differences in the physical structures and dynamics of two adjacent maar lakes at Mt. Vulture volcano. Geochem Geophys Geosyst 14
12. Cabassi J, Tassi F, Vaselli O, Fiebig J, Nocentini M, Capecchiacci F, Rouwet D, Bicocchi G (2013) Biogeochemical processes involving dissolved CO_2 and CH_4 at Albano, Averno, and Monticchio meromictic volcanic lakes. Bull Volcanol 75
13. Tassi F, Vaselli O, Tedesco D, Montegrossi G, Darrah T, Cuoco E, Mapelli F, Borin S, Rouwet D (2009) Water and gas chemistry at Lake Kivu. Geochem Geophys Geosyst 10
14. Aeschbach-Hertig W, Hofer M, Kipfer R, Imboden DM, Wieler R (1999) Accumulation of mantle gases in a permanently stratified volcanic lake (Lac Pavin, France), Geochim. Cosmochim Ac 63:3357–3372
15. Camus G, Michard G, Olive P, Boivin P, Desgranges P, ez equel J, Meybeck D, Peyrus M, Vinson JC, Viollier JM, E., and, Kornprobst J (1993) Risques d'eruptions gazeuse carbonique en Auvergne. B Soc Geol Fr 164:767–781
16. Bahrig B (1988) Palaeoenvironment information from deep water siderite (Lake of Laach, West Germany). Geol Soc Lond Spec Publ 40:153–158
17. Sime-Ngando T, Boivin P, Chapron E, Jezequel D, Meybeck M (2016) Lake Pavin. History, geology, biogeochemistry, and sedimentology of a deep meromictic maar lake. (ed), XV. Springer, p. 421
18. Schmid M, Halbwachs M, Wehrli B, Wüest A (2005) Weak mixing in Lake Kivu. Geochem Geophys Geosyst 6:Q07009

19. Cabassi J, Tassi F, Mapelli F, Borin S, Calabrese S, Rouwet D (2014) Geosphere-biosphere interactions in bio-activity volcanic lakes: evidences from Hule and Río Cuarto (Costa Rica). PLoS ONE 9:e102456
20. Mouhamed AN, Rouwet D, Tassi F, Fantong WY, Mouncherou OF, Ekomane E, Fagel N (2023) Evidence of Lake Nyos-type behavior in the geological record: A review. Earth-Sci Rev 247:104603. https://doi.org/10.1016/j.earscirev.2023.104603
21. Asaah ANE, Yokoyama T, Iwamori H, Aka FT, Kuritani T, Usui T (2021) High signature in lavas of Mt. Oku: implications for lithospheric and asthenospheric contributions to the magmatism of the Cameroon Volcanic Line West Africa. Lithos 400–401:106416. https://doi.org/10.1016/j.lithos.2021.106416
22. Schmidt C, Laag C, Whitehead M, Profe J, Aka FT, Hasegawa T, Kereszturi G (2022) Complexities of assessing volcanic hazards along the Cameroon Volcanic Line. J Volcanol Geotherm Res 427:107558
23. Fouepe TA, Romaric N, Kazuto S, Ohba T, Kamtchueng B, Tanyileke G, Benoit F, Hell J (2019) New insights into volume estimates and gas contents from acoustic investigation at Lake Monoun. J Afr Earth Sci 160:103604
24. Ohba T, Oginuma Y, Saiki K, Kusakabe M, Issa, Fouepe TA, Ntchantcho R, Tanyileke G, Hell JV (2022). A depression filled with CO_2 enriched water in Lake Monoun. Front Earth Sci 10:766791
25. Nche LA, Hasegawa T, Aka FT, Ohba T, Mafany GT, Németh K, Miyabuchi Y, Kaneda Y, Asaah ANE (2025) Volcanic history and magma systems of Lake Monoun Polygenetic Maar. J Volcanol Geotherm Res 460
26. Kusakabe M, Ohba T, Issa Y, Yoshida Y, Satake H, Ohizumi T (2008) Evolution of CO_2 in Lakes Monoun and Nyos. Geochem J 42:93–118
27. Schnellmann M, Anselmetti FS, Giardini D, McKenzie JA (2005) Mass movement-induced fold-and-thrust belt structures in unconsolidated sediments in Lake Lucerne (Switzerland). Sedimentology 52:271–289
28. Xie M, Ma F, Chen G, Zheng X, Xiao R, Zhang C (2023) Genesis and geological significance of siderite in the Nantun Formation. Minerals 13:804
29. Ohmoto H, Watanabe Y, Kumazawa K (2004) Evidence from massive siderite beds for a CO2-rich atmosphere before ~ 1.8 billion years ago. Nature 429:395–399. https://doi.org/10.1038/nature02573
30. Bahrig B (1989) Stable isotope composition of siderite as an indicator of the paleoenvironmental history of oil shale lakes,Palaeogeography, Palaeoclimatology. Palaeoecology 70(1–3):139–151. https://doi.org/10.1016/0031-0182(89)90085-0
31. Bernard A, Symonds RB (1989) The significance of siderite in the sediments from Lake Nyos. Cameroon J Volcanol Geotherm Res 39:187–194
32. Hodgkinson J, Cox ME, McLoughlin S (2008) Coupling mineral analysis with conceptual groundwater flow modelling: The source and fate of iron, aluminium and manganese in a back-

barrier island. Chem Geol 251(1–4):77–98

33. Roh Y, Zhang CL, Vali H, Lauf RJ, Zhou J, Phelps TJ (2003) Biogeochemical and environmental factors in Fe biomineralization. Clays Clay Min 51:83–95
34. Kouokam SC, Wotchoko P, Suh CE, Chako-Tchamabé B, Vohnyui CM-L, Suh GC, Yetoh FW, Mouncherou FO (2025) Pre-eruptive CO2-rich fluid interactions and siderite genesis at the Monoun Maar Volcano, Cameroon Volcanic Line: insights from stable carbon and oxygen systematics. Earth Sci 14:160–171
35. Bertrand S, Tjallingii R, Kylander ME, Wilhelm B, Roberts SJ, Arnaud F, Brown E, Bindler R (2024) Inorganic geochemistry of lake sediments: A review of analytical techniques and guidelines for data interpretation. Earth-Sci Rev 249:104639
36. Fagel N, Israde-Alcantara I, Safaierad R, Rantala M, Schmidt S, Lepoint G, Pellenard P, Mattielli N, Metcalfe S (2024) Environmental significance of kaolinite variability over the last centuries in crater lake sediments from Central Mexico. Appl Clay Sci 247:107211. https://doi.org/10.1016/j.clay.2023.107211
37. Ece ÖI, Ercan HÜ (2024) Global occurrence, geology and characteristics of hydrothermal origin kaolin deposits. Minerals 14:353
38. Usman UA, Yusoff I, Raoov M et al (2021) Natural sources of iron and manganese in groundwater of the lower Kelantan River Basin, North-eastern coast of Peninsula Malaysia: water quality assessment and an adsorption-based method for remediation. Environ Earth Sci 80:425. https://doi.org/10.1007/s12665-021-09717-0
39. Heiri O, Lotter AF, Lemcke G (2001) Loss on ignition as a method for estimating organic and carbonate content in sediments. J Paleolimnol 25:101–110
40. Moore DM, Reynolds RC, Jr (1997) X-Ray Diffraction and the Identification and Analysis of Clay Minerals. Oxford University Press, Oxford, p 332
41. Reimer PJ, Austin WE, Bard E, Bayliss A, Blackwell PG, Ramsey CB, Butzin M, Cheng H, Edwards RL, Friedrich M (2020) The IntCal20 radiocarbon age calibration curve. Radiocarbon 62:725–757
42. Blaauw M, Christen JA, Aquino López MA, Esquivel Vázquez J, Gonzalez OM, Belding T, Theiler J, Gough B, Karney C (2021) rbacon: Age-depth modelling using Bayesian statistics. CRAN
43. R Core Team. R: A Language and Environment for Statistical Computing. R Foundation for Statistical Computing, Vienna, Austria (2024) https://www.R-project.org/

Figures

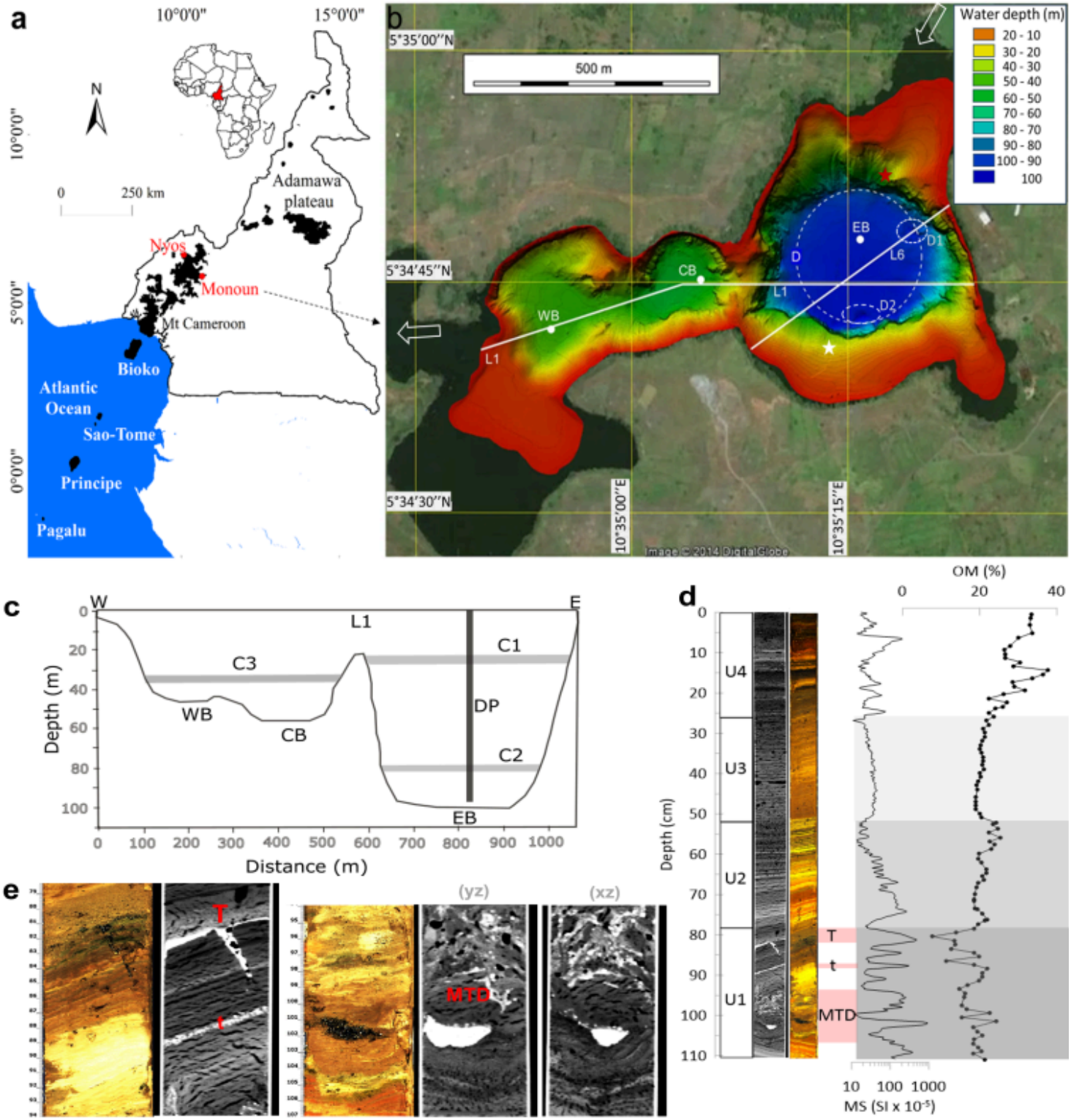


Figure 1

Location, bathymetry, and sedimentological features of Lake Monoun.

a Location of Lake Monoun in Cameroon. Black areas show the Cameroon Volcanic Line, extending from the Atlantic Ocean to northern Cameroon, and red dots mark Lakes Nyos and Monoun. **b** Bathymetric map of Lake Monoun, modified after Ohba et al.[24]. WB, western basin; CB, central basin (46 m depth); EB,

eastern basin (56 m depth); L1, transect shown in **c**; L6, transect shown in Fig. 6; D, perimeter of the diatreme; D1 and D2, depressions. White and red stars mark the locations of cores LMo23-2 and LMo23-1, respectively; LMo23-1 is not discussed further in the text. **c** Cross-section along line L1. DP, artificial degassing pipe (97 m long); C1, shallow chemocline observed in 2003; C2 and C3, chemoclines observed in 2015[24,26]. **d** Sedimentological description of core LMo23-2, showing, from left to right, sedimentary units, CT images, core photographs, and downcore variations in magnetic susceptibility (MS) and organic matter (OM). **e** Close-up views of distinctive sedimentological features, including a mass-transport deposit (MTD, CT sections in the *y-z* and *x-z* planes), a possible tephra layer (t), and a turbidite (T).

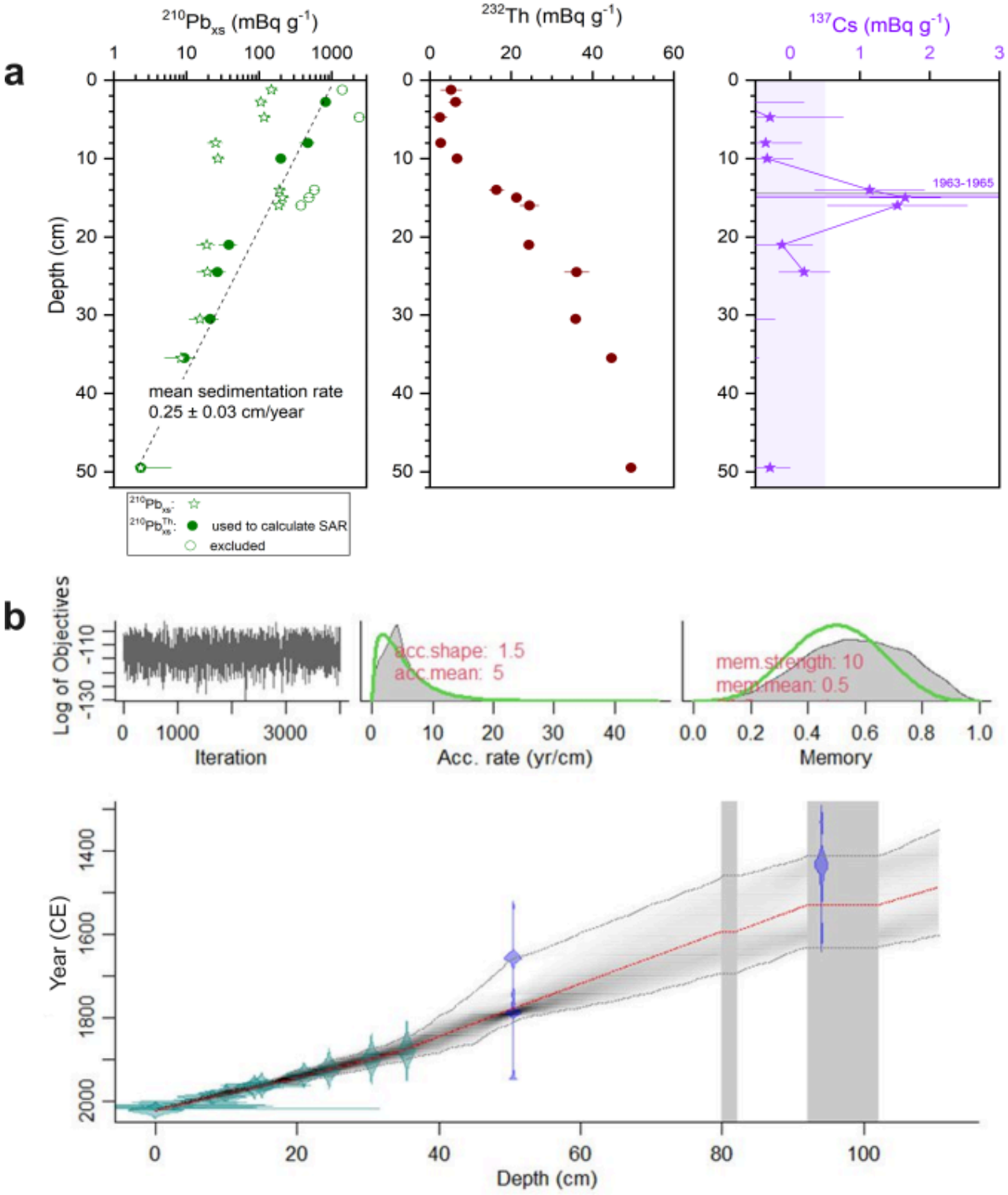


Figure 2

Age-depth model for core LMo23-2.

a Age model derived from radionuclide measurements in the upper part of core LMo23-2. Left panel: open stars, measured $^{210}Pb_{xs}$ data reported vs. core depth; green circles, $^{210}Pb_{xs}$ data normalised by ^{232}Th (i.e. $^{210}Pb_{xs}$ - ^{232}Th) and used to calculate the sediment accumulation rate (SAR); open circles,

points excluded for the SAR calculation due to their abnormally high $^{210}Pb_{xs}$ values or low resolution. Middle panel: measured ^{232}Th data reported vs. core depth. Right panel: measured ^{137}Cs data reported vs. core depth. **b** Bayesian age-depth model based on the $^{210}Pb_{xs}$-derived SAR and ^{14}C ages. The upper panels illustrate the iterations of the Markov Monte Carlo chain (left) and the Bayesian parameter distributions with the priors in green and the posteriors in gray (middle, right). In the bottom panel, the red line shows mean age estimates, with the 95% confidence intervals reported as the gray error envelope. Green distributions represent ^{210}Pb ages. The distributions of ^{14}C ages at 50.5 and 94 cm depth in core are shown in blue. The two gray bands (82–79 and 102–93 cm depth in core) represent the mass deposits that were removed from the model.

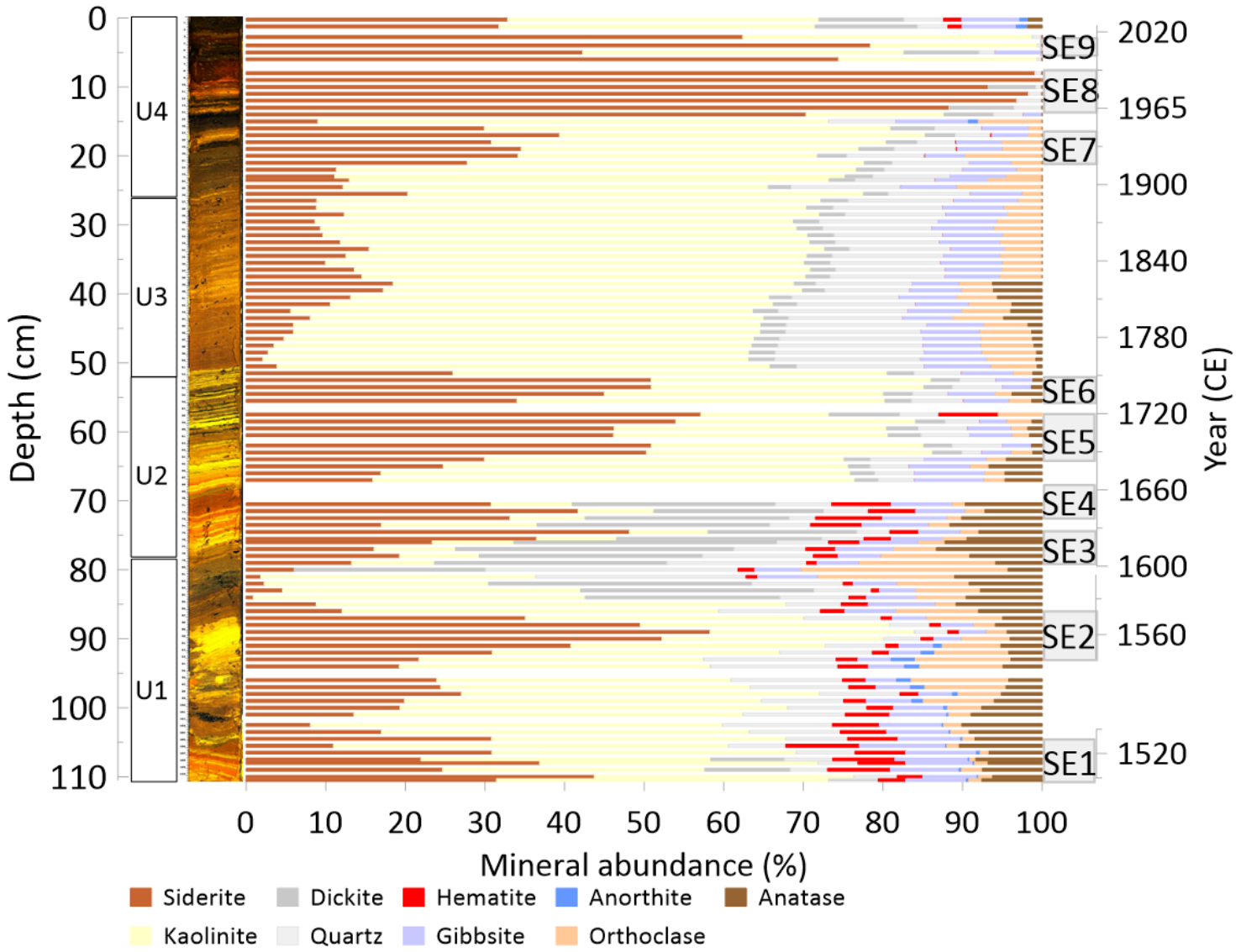


Figure 3

Mineralogical evolution in core LMo23-2.

The nine siderite-rich intervals (SE1 to SE9) are marked on the right-hand side. Notably, dominantly to exclusively siderite sediments occurs in SE8 around the time of the 1984 limnic eruption.

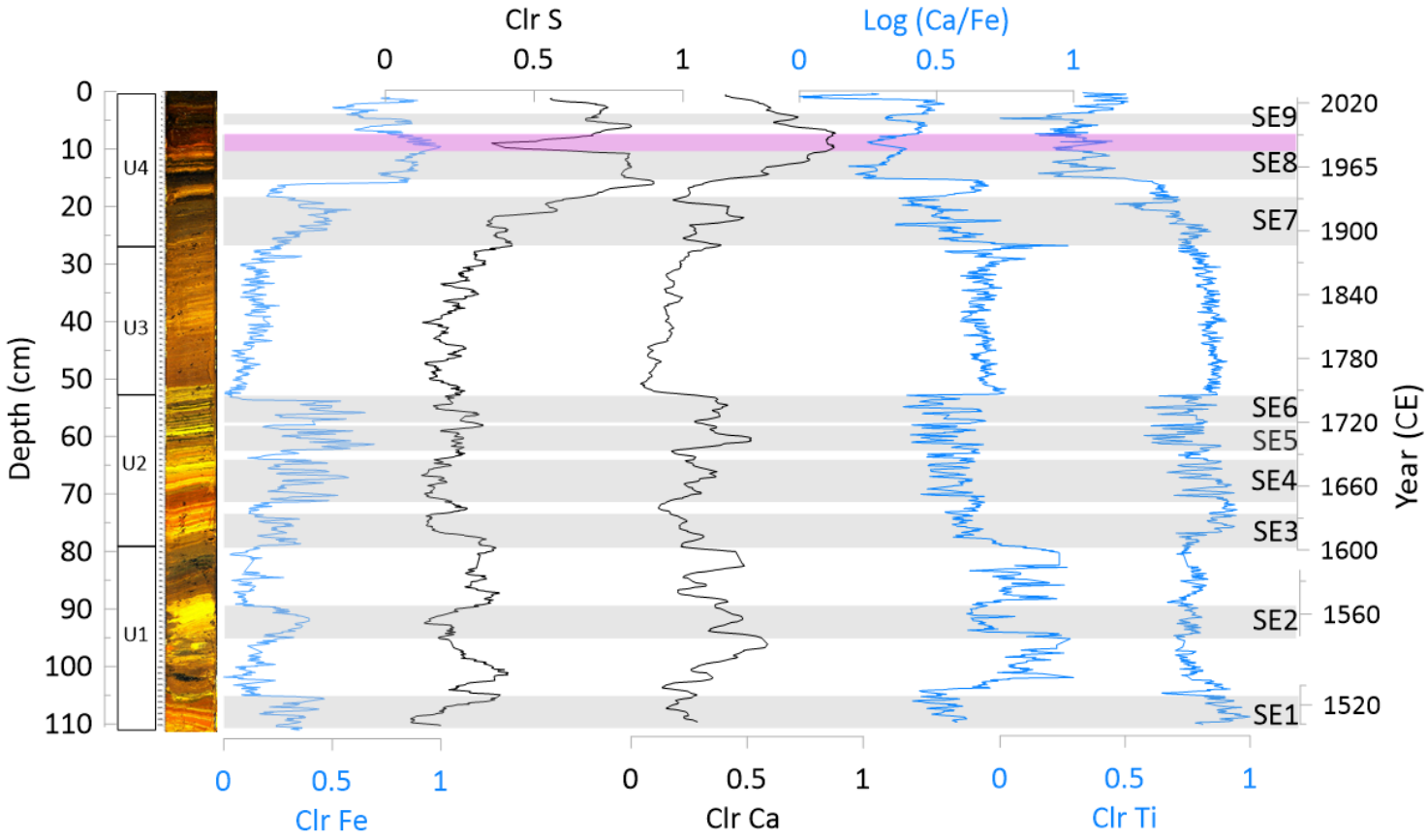


Figure 4

Geochemical variations in core LMo23-2.

Element intensities were centered log-ratio (clr) transformed and min-max normalized. Black curves show five-point moving averages. The nine siderite-rich intervals (SE1–SE9) are indicated by gray horizontal bands. The purple horizontal band marks the end of SE8.

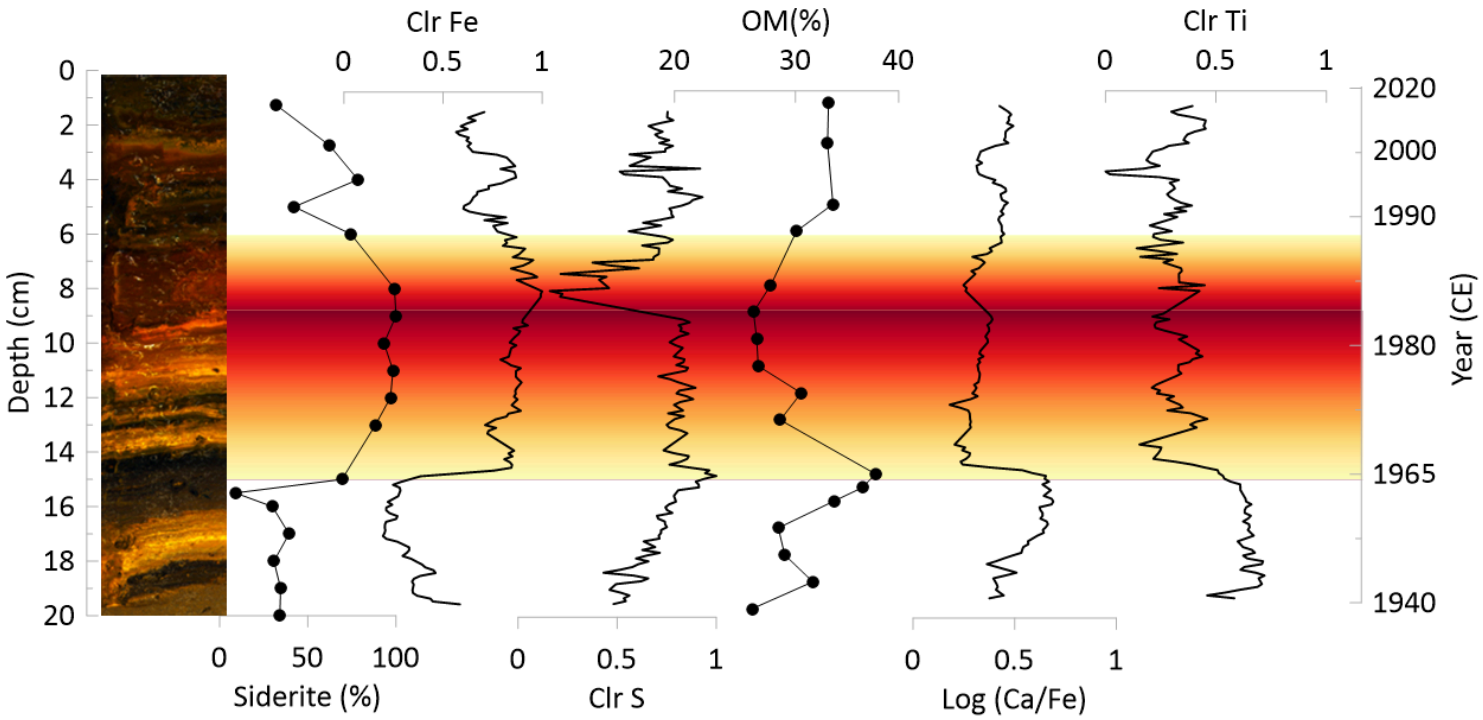


Figure 5

Mineralogical, geochemical and sedimentological variations in core LMo23-2 associated with the 1984 limnic eruption.

The yellow to dark red band highlights distinct changes in the sediments occurring before and after the limnic eruption (indicated by the dark line).

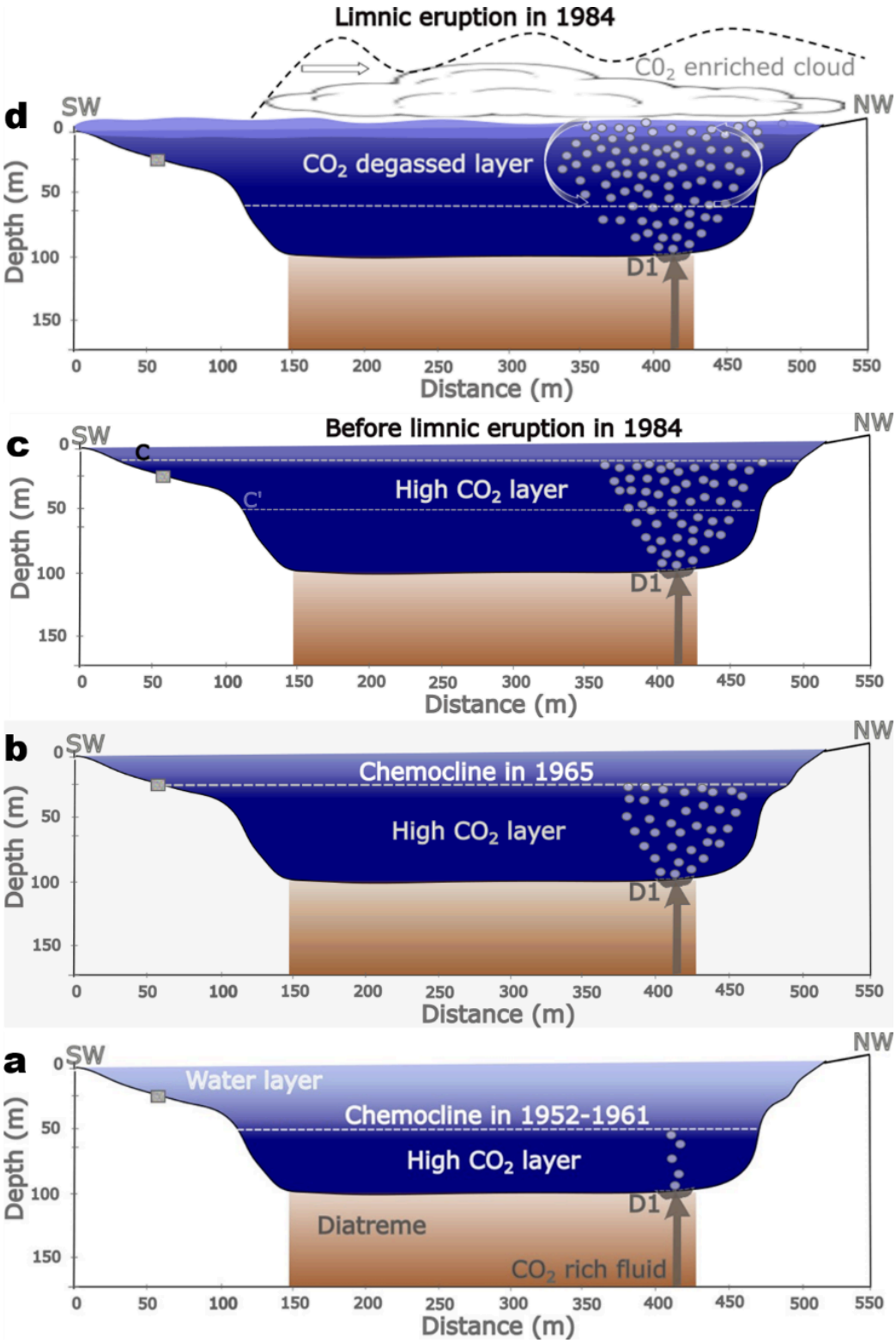


Figure 6

Schematic model of Lake Monoun before and during the 1984 limnic eruption.

The small gray square on the left marks the position of core LMo23-2, collected at a water depth of 25 m. **a** Stage 1: CO_2-rich fluid ascending along the annular fault of the diatreme enters the lake bottom through depression D1, accompanied by gas bubbles. Deep waters contain high dissolved CO_2

concentrations, and the chemocline is at ~50 m depth[24,26]. **b** Stage 2: continued CO_2 influx displaces the chemocline to shallower than 25 m depth. **c** Stage 3: shortly before the limnic eruption, continued CO_2 influx further displaces the chemocline to ≤15 m depth (C). C' indicates the chemocline proposed in the previous model of Ohba et al.[24]. **d** Stage 4: limnic eruption. Rupture of the chemocline leads to mixing of the water layers. CO_2-rich water rises towards the surface, generating a wave, while CO_2 clouds spread laterally by gravity across the surrounding land.

Supplementary Files

This is a list of supplementary files associated with this preprint. Click to download.

- SupplementarymaterialsforE.L.ENature.pdf